JAERI-Research--94-034

JP9501212

JAERI-Research
94-034

NUMERICAL PREDICTION ON TURBULENT HEAT TRANSFER OF A SPACER RIBBED FUEL ROD FOR HIGH TEMPERATURE GAS-COOLED REACTORS

November 1994

Kazuyuki TAKASE

日本原子力研究所
Japan Atomic Energy Research Institute

本レポートは，日本原子力研究所が不定期に公刊している研究報告書です

入手の問合わせは，日本原子力研究所技術情報部情報資料課（〒319-11 茨城県那珂郡東海村）あて，お申し越しください．なお，このほかに財団法人原子力弘済会資料センター（〒319-11 茨城県那珂郡東海村日本原子力研究所内）で複写による実費頒布をおこなっております

This report is issued irregularly.

Inquiries about availability of the reports should be addressed to Information Division, Department of Technical Information, Japan Atomic Energy Research Institute, Tokai-mura, Naka-gun, Ibaraki-ken 319-11, Japan.

編集兼発行　日本原子力研究所

印　　刷　㈱原子力資料サービス

Numerical Prediction on Turbulent Heat Transfer of a Spacer Ribbed Fuel Rod for High Temperature Gas-cooled Reactors

Kazuyuki TAKASE

Department of High Temperature Engineering
Tokai Research Establishment
Japan Atomic Energy Research Institute
Tokai-mura, Naka-gun, Ibaraki-ken

(Received October 11, 1994)

The turbulent heat transfer of a fuel rod with three-dimensional trapezoidal spacer ribs for high temperature gas-cooled reactors was analyzed numerically using the k-ε turbulence model, and investigated experimentally using a simulated fuel rod under the helium gas condition of a maximum outlet temperature of 1000 ℃ and pressure of 4 MPa. From the experimental results, it found that the turbulent heat transfer coefficients of the fuel rod were 18 to 80 % higher than those of a concentric smooth annulus at a region of Reynolds number exceeding 2000. On the other hand, the predicted average Nusselt number of the fuel rod agreed well with the heat transfer correlation obtained from the experimental data within a relative error of 10 % with Reynolds number of more than 5000. It was verified that the numerical analysis results had sufficient accuracy. Furthermore, the numerical prediction could clarify quantitatively the effects of the heat transfer augmentation by the spacer rib and the axial velocity increase due to a reduction in the annular channel cross-section.

Keywords: Convective Heat Transfer, Gas-cooled Reactors, Annular Channel, Fuel Rod, Spacer Ribs, Turbulent Analysis, Experimental Data, Numerical Prediction, Heat Transfer Augmentation.

高温ガス炉用スペーサリブ付き燃料棒の乱流熱伝達に関する数値予測

日本原子力研究所東海研究所高温工学部
高瀬　和之

（1994年10月11日受理）

3次元の台形状をしたスペーサリブを表面に持つ高温ガス炉用燃料棒の乱流熱伝達を，k-ε乱流モデルを使って数値的に解析した。また，出口最高温度1000℃，圧力4 MPaのヘリウムガス条件のもとで模擬燃料棒を使って実験的に調べた。実験の結果，燃料棒の乱流熱伝達率は2000を超えるレイノルズ数域では，平滑環状流路の値よりも18％から80％も上昇することがわかった。一方，燃料棒の平均ヌッセルト数の計算値は，実験データから得られた熱伝達相関式に対して5000以上のレイノルズ数域では10％の相対誤差で良く一致し，本計算結果は十分な精度を有していることを確認した。さらに，スペーサリブによる伝熱促進効果や流路断面積減少による軸方向流速増大の影響を数値計算によって定量的に明らかにした。

東海研究所：〒319－11　茨城県那珂郡東海村白方字白根2－4

Contents

目　　次

1. Introduction

Japan Atomic Energy Research Institute (JAERI) has been constructing a High Temperature Engineering Test Reactor (HTTR) to establish and upgrade technology for very high temperature gas-cooled reactors (VHTR) and is promoting innovative high temperature research. The HTTR is a helium-cooled, graphite-moderated reactor with inlet temperature of 395°C, maximum outlet temperature of 950°C, pressure of 4 MPa and thermal output power of 30 MW. Figure 1 shows a fuel element installed in the core of the HTTR. The HTTR core consists of 30 and 5 fuel elements installed horizontally and vertically, respectively. The fuel element consists of a hexagonal graphite block with 33 fuel holes and 33 fuel rods. The fuel rod is inserted into the fuel hole. Helium gas flows downward into each fuel channel, which is an annular passage between the fuel hole and the external surface of the fuel rod, with an annulus ratio of 0.829. In addition, its Reynolds number, Re, from the fuel channel inlet to the outlet is between 10000 and 3000.

The thermal-hydraulic performance of the fuel rod for the VHTR has already evaluated by JAERI using a simulated fuel rod under a maximum outlet helium gas temperature of 700°C and an annulus ratio of 0.868 [1]. However, as for studies on the turbulent heat transfer in annular passages, Kays and Leung [2] mainly considered analytically the heat transfer coefficients of the smooth annulus for wide ranges of Re, annulus ratio and Plandtl number, Pr. Dalle Donne et al. [3] , [4] derived empirical correlations for the fuel rod with/without rectangular ribs, Wilson and Medwell [5] analyzed the heat transfer phenomena for fully developed turbulent flows in concentric smooth annuli, Hassan and Rehme [6] investigated the heat transfer in rod bundles with spacer grids, and Takase et al. [7] evaluated experimentally and numerically the heat transfer characteristics of the annular fuel channel with two-dimensional square ribs. Furthermore, Han et al. [8] investigated the effects of the shape of the ribs, attack angle and ratio of rib pitch to height regarding heat transfer in a rib-roughened rectangular duct.

However, every experimental condition of the previous research, such as temperature, pressure, Re, heat flux and annulus ratio, does not perfectly simulate the HTTR operational conditions. In particular, the basic difference between the previous research and the present study is the geometry of the annular passage. As shown in Fig. 1, the fuel rod for the HTTR has a total of nine three-dimensional trapezoidal roughness, so-called spacer rib, on its outer surface so as to keep the concentricity of the annulus. From the viewpoint of nuclear reactor safety, it is risky to estimate the heat transfer performance of the fuel rod for the HTTR from

the results of previous research. Therefore, to determine the thermal performance for a HTTR core, the heat transfer coefficients and the friction factors of the fuel rod for the HTTR were investigated by thermal-hydraulic demonstration experiments using the same helium gas condition as the HTTR operation. On the other hand, no one has analyzed numerically the turbulent heat transfer of the spacer ribbed annular channel up to now, so that the author [9] carried out its numerical prediction using a three-dimensional computation and the k-ε turbulence model. In this analysis, the boundary coordinate fitted method was adopted due to simulate the shape of the spacer rib.

2. Experimental Investigation

2.1 Experimental Conditions

Figure 2 shows a schematic drawing of a test rig and measuring positions of temperature, pressure and differential pressure. Helium gas supplies from a circulator through a flow meter into a pressure vessel of the test rig. Then, it goes into the fuel channel after the fluid temperature was adjusted by a preheater installed in the upper plenum, and it is heated up to 1000°C at maximum temperature by the fuel rod at the measuring section and cooled down to less than 400°C by an internal cooler in the lower plenum, and finally returns to the circulator. According to the experimental conditions, the helium gas flow rate, G, was measured by one of three flow meters with full measuring ranges of 7, 18 and 50 g/s, respectively. The accuracy of each flow meter was within ±0.2% for the full measuring range. In addition, the electric power, which was supplied to the fuel rod, was measured using an electric power meter with a full measuring range of 120 kW. Its accuracy was ±0.25% for the full measuring range.

The outer tube was made of Incolloy 800H with high-melting temperature, and it was 41 mm in inner diameter, Do, 5 mm in thickness and 6370 mm in length. The fuel rod diameter, Di, was 34 mm, so that a hydraulic diameter, De, obtained from Do-Di was 7 mm and the gap width between the fuel rod and the outer tube was 3.5 mm. They were the same as the HTTR conditions. The outer tube was surrounded by a fibrous thermal insulation with a thickness of 70 mm, and its outside was encircled with compensating heater blocks to minimize the heat loss in the radial direction. Nine K thermocouples sheathed with an Inconel 600 tube with an outer diameter of 3.2 mm and ten pressure taps with an inner

diameter of 1 mm, were embedded onto the outer tube wall to measure the outer wall temperature, T_{cw}, and the axial pressure drop, Δp. At each position of the inlet and outlet measuring sections, the static pressure of the helium gas, P, was measured by a pressure transducer with a full measuring range of 4.5 MPa. The measuring section was divided into nine sub-sections, seven heated and two non-heated ones. Here, the former means the active core for the HTTR and the later the removal reflectors, respectively. The Δp of each sub-section was measured by two differential pressure transducers with full measuring ranges of 1 and 5 kPa, according to the experimental conditions. The measuring accuracy of each transducer was within ±0.2% for the full measuring range.

A simulated fuel rod for the HTTR, as shown in Fig. 3, was an electrical heater with a maximum electric power of 100 kW with uniform axial heat flux distribution. It consisted of seven sub-rods, upper and lower electrodes. The sub-rod consisted of a graphite sleeve, a boron-nitride insulation, and a coiled graphite heating element. The graphite sleeve was 570 mm in length and 460 mm in effective heating length. On its outer surface, so as to keep the constant annular gap width in the flow direction, three spacer ribs were set linearly in the upper, center and lower axial positions. In addition, as for these axial positions, three spacer ribs were set at an angle of 120° in the circumferential direction. Therefore, the total number of the spacer rib was nine per sub-rod. The normal tolerance between the inner diameter of the outer tube and the outer diameter of the spacer ribs was less than 0.3 mm.

The fuel rod surface temperature, T_w, that was the same meaning as the inner wall temperature of the annular channel, was measured by 13 K thermocouples sheathed with an Inconel 600 tube with an outer diameter of 1.6 mm. Two thermocouples were set at positions of 172 mm and 407 mm from the top of each sub-rod, except for the 7th stage sub-rod. Only one thermocouple was installed at the position of 172 mm from the top of the 7th stage sub-rod. The lead wires of those thermocouples were laid on the inner surface of the graphite sleeve using grooves. Then, the hot junction of each thermocouple was taken out from the inner to the outer surfaces at the measuring position. The bulk temperature, T_b, was measured at the inlet and outlet positions of the annular channel; the channel inlet bulk temperature, $T_{b,i}$, was measured by a K thermocouple sheathed with an Inconel 600 tube with an outer diameter of 1.6 mm at a position 270 mm higher than the top of the simulated fuel rod. On the other hand, the channel outlet bulk temperature, $T_{b,o}$, was measured by three K thermocouples sheathed with an Inconel 600 tube with an outer diameter of 3.2 mm at a position 135 mm lower than the bottom of the simulated fuel rod. They were installed at the same elevation to measure the temperature deviation in the circumferential direction.

The uncertainty of every temperature measurement was estimated to be within ±1.5 °C of the measured value.

The experiments were carried out under the conditions of $T_{b,i}$=135 - 225°C, P=4 MPa, G=3-20 g/s, Re=2100 - 15900 at the annular channel inlet, and 9 - 60 kW in electric input for the simulated fuel rod. Furthermore, a dimensionless heat flux parameter at the channel inlet, q^*_i, was $1.48\times10^{-3} < q^*_i < 1.95\times10^{-3}$. The q^*_i was specified by

$$q_i^* = \frac{q_e}{Gc_p(T_b + 273.15)} \frac{\pi(Do^2 - Di^2)}{4} \tag{1}$$

Where, q_e is the total heat flux calculated from the electric heat generation rate along the axial direction, and c_p thermal conductivity of the fluid. The q^*_i of the HTTR is nearly equal to 0.9×10^{-3}, so that the q^*_i of the present study is from 1.64 to 2.16 times higher than that of the HTTR.

2.2 Results and Discussion

As an example of axial temperature distributions, Fig. 4 shows the inner and outer wall temperature distributions which were obtained from a series of experiments in the laminar, transition and turbulent regions. Where, x/De means the dimensionless axial distance, x the axial distance from the channel inlet, T_{iw} and T_{ow} the inner and outer wall temperatures, and Re_i and Re_o the channel inlet Re and the channel outlet Re, respectively. From this figure, it can be seen that the radiative heat transfer is effective regarding the total heat transfer because both surfaces have a high temperature. The radiative heat flux, q_r, from the fuel rod surface to the outer tube wall was calculated by

$$q_r = \sigma\left(T_{iw}^4 - T_{ow}^4\right)\left[\frac{1}{\varepsilon_{iw}} + \frac{Di}{Do}\left(\frac{1}{\varepsilon_{ow}} - 1\right)\right]^{-1} \tag{2}$$

Where, σ is Stefan-Boltzmann's constant, ε_{iw} and ε_{ow} emissivities for the fuel rod surface and for the outer tube wall. For the temperature range in the present study, ε_{iw} and ε_{ow} are 0.8 in graphite [10] and 0.3 in Incolloy 800H [11], respectively. Therefore, convective heat flux, q_c, is obtained by $q_c = q_e - q_r$.

Figure 5 shows the relation between q_r/q_c and Re, where q_r/q_c means the ratio of radiative and total heat fluxes. The q_r/q_c increased as x/De increased because the temperature level was high, and it reached to more than 10% when Re<2500 at x/De=288. In the HTTR, the graphite blocks are used as the component material for the fuel channel, so that it was expected that the q_r/q_c at the HTTR core was larger than that of the present results.

Figure 6 shows the relation between local Nusselt number, Nu, and local Re in a fully developed flow region. The open symbol indicates the Nu of the fuel rod, Nu_f, obtained from experimental data, and the Nu_f was calculated by

$$Nu = q_c De/\lambda (T_{hw} - T_{bm}) \qquad (3)$$

Where, T_{bm} is the bulk average temperature, λ thermal conductivity of helium gas evaluated by the T_{bm}. The broken line shows the Nu of the concentric smooth annulus, Nu_s, and those correlations are represented by the following equations:

$$Nu_s = 0.018(Di/Do)^{-0.16} Re^{0.8} Pr^{0.4} \quad ; Re \geq 7000 \quad [3]$$

$$Nu_s = 0.084(Re^{2/3} - 110)Pr^{0.4} \quad ; 2700 < Re < 7000 \quad [12]$$

$$Nu_s = 5.6 \quad ; Re \leq 2700 \quad [13]$$

The Nu_f was much larger than the Nu_s from the laminar to the turbulent Re regions. It was approximately 25% higher than the Nu_s in the laminar region, similarly 18% higher in the turbulent region and a maximum of 80% higher in the transition region. As the reason for those heat transfer augmentations, it was mainly thought that the spacer ribs contributed effectively as turbulence promoters. On the other hand, as the Re decreased from the turbulent to the laminar regions, the following special feature was observed: the Nu_s decreased suddenly as soon as Re was less than about 7000; however, the Nu_f decreased as a straight line with Re. This means that the transition region of the fuel rod was very small in comparison with the concentric smooth annulus. Consequently, the following empirical correlations for the fuel rod were derived from all experimental data in the turbulent region of Re>2000 and the laminar region of Re≤1800.

$$Nu_f = 0.0219 Re^{0.8} Pr^{0.4} \quad ; Re > 2000 \tag{4}$$

$$Nu_f = 7.0 \quad ; Re \leq 1800 \tag{5}$$

Equations. (3) and (4) are shown as solid lines in Fig. 6. They agreed very well with the experimental data within a relative error of 6%.

3. Numerical Analysis

3.1 Governing Equations

As proposed by Patankar, Liu and Sparrow [14], the pressure, P, in periodic fully developed flows can be expressed as

$$P(x, y, z) = -\beta x + P_p(x, y, z) \tag{6}$$

Where, β is the mean pressure gradient, $P_p(x, y, z)$ the periodic part of pressure, βx the pressure drop that takes place in the flow direction, x, y and z axial, radial and circumferential coordinates, respectively. Similarly, the temperature, T, can be written as

$$T(x, y, z) = \gamma x + T_p(x, y, z) \tag{7}$$

Where, γ is the mean temperature gradient, $T_p(x, y, z)$ the periodic part of temperature, γx the rate of temperature rise in the flow direction.

The governing equations can be written as:

continuity

$$\frac{\partial}{\partial x_i}(\rho u_i) = 0 \tag{8}$$

momentum

$$\frac{\partial}{\partial x_j}(\rho u_i u_j) = -\frac{\partial p_p}{\partial x_i} + \frac{\partial}{\partial x_j}\left[\mu_{eff}\left(\frac{\partial u_i}{\partial x_j} + \frac{\partial u_j}{\partial x_i}\right)\right] - \frac{2}{3}\mu_{eff}\frac{\partial u_l}{\partial x_l} + \beta \tag{9}$$

energy

$$\frac{\partial}{\partial x_i}(\rho u_i c_p T_p) = \frac{\partial}{\partial x_i}\left(\frac{c_p \mu_{eff}}{Pr_t}\frac{\partial T_p}{\partial x_i}\right) - \rho u_i c_p \gamma \tag{10}$$

turbulent kinematic energy, k

$$\frac{\partial}{\partial x_i}(\rho u_i k) = \frac{\partial}{\partial x_i}\left(\frac{\mu_{eff}}{\sigma_k}\frac{\partial k}{\partial x_i}\right) + \mu_t\left(\frac{\partial u_i}{\partial x_j} + \frac{\partial u_j}{\partial x_i}\right)\frac{\partial u_i}{\partial x_i} - \rho\varepsilon \tag{11}$$

turbulent dissipation rate, ε

$$\frac{\partial}{\partial x_i}(\rho u_i \varepsilon) = \frac{\partial}{\partial x_i}\left(\frac{\mu_{eff}}{\sigma_\varepsilon}\frac{\partial \varepsilon}{\partial x_i}\right) + C_{\varepsilon 1}\mu_t\frac{\varepsilon}{k}\left(\frac{\partial u_i}{\partial x_j} + \frac{\partial u_j}{\partial x_i}\right)\frac{\partial u_i}{\partial x_i} - C_{\varepsilon 2}\rho\frac{\varepsilon^2}{k} \tag{12}$$

Where, u is velocity component, subscripts i, j, l Einestein's suffixes, and C_μ, $C_{\varepsilon 1}$, $C_{\varepsilon 2}$, σ_κ, σ_ε turbulence model constants which were taken by Jones and Launder [15].

3.2 Numerical Conditions

Figure 7 shows an analytical model and the boundary conditions. It simulates a part of the fuel channel at the arbitrary axial location from the inlet to the outlet of the annulus. The computation was performed for one periodic axial length in a three-dimensional annular channel with a central angle of 120°.

The fluid flows from the upper to lower in the annular channel. To obtain a fully developed turbulent flow at the inlet of the analytical domain, the periodic boundary condition was set at the inlet and outlet sections. The calculated values of velocities and turbulence quantities at the outlet section were substituted as the inlet conditions for the next iteration. Furthermore, the symmetric boundary condition was set to both circumferential ends of the analytical domain. Here, the sector angle between the symmetric boundary and the center of the spacer rib was 60°. The u, v and w in Fig. 7 were fluid velocity components corresponding to the x, y and z directions, respectively. At the walls, $u=v=w=0$. The constant heat flux was given for every wall, but its thermal conduction was neglected. The radiation from the inner to outer walls was also considered. The wall function, that was a log-law when $y^+>11.6$ and a linear-law when $y^+\leq 11.6$, was specified as the wall boundary condition. Here, the y^+ was defined as $y^+=\rho y_p C_\mu^{1/4} k_p^{1/2}$ and subscript p referred to the grid point adjacent to the wall. The near-wall dissipation value was prescribed as $\varepsilon=C_\mu^{3/4}k^{3/2}/\kappa y_p$ from the equilibrium assumption in which the production and dissipation of turbulence were

equal. Here, κ is the Karmann's constant. The wall gradient of k was also set to zero. The wall temperature, T_w, was obtained from the following formulation [16] that was based on the analogy between heat and momentum transfer.

$$\frac{\lambda[(T_w - T_b)/y_p]}{q_c} = \frac{1}{\kappa y^+}\frac{Pr_t}{Pr}\ln(Ey^+) + \frac{1}{y^+}\left(\frac{Pr_t}{Pr}\right)^{5/4}\frac{(\pi/4)}{\sin(\pi/4)}\left(\frac{C_D}{\kappa}\right)^{1/2}\left(\frac{Pr_t}{Pr} - 1\right) \qquad (13)$$

Here, E and C_D mean the log-law constant and the van Driest's constant, respectively.

The numerical analysis condition simulated one of experimental conditions, and it was as follows: the fluid was helium gas with an inlet temperature of 500 °C and inlet pressure of 4 MPa. The heat flux for the inner wall and the spacer rib surface was 62.6 kW/m^2, the outer wall was insulated, the emissivity for the inner wall and the spacer rib surface was 0.8, the emissivity for the outer wall was 0.3, and the inlet average Re varied from 3000 to 20000. The FLUENT [17] that was a thermal-hydraulic analysis code was used in this study. Its computational algorithm was based on the SIMPLE [18] method using the control volume finite difference procedure. In the governing equations, convective and diffusion terms were discretized using the power-law and the central differencing schemes, respectively. Then, the discretized equations were solved using the Multi-grid method [19]. A boundary coordinate fitted method was adopted to generate arbitrary grid points which would fit the shape of analytical body surface. Thus, the computation was performed transforming the analytical domain in Fig. 7 to the computational domain that was shown as a rectangular solid. The computational grid consisted of 45x8x51 points in the x, y and z directions. A procedure and equations for the coordinate transformation used to the present study are described in Ref.[20].

3.3 Thermophysical Properties

An assumption of the constant fluid properties is not adequate under the condition that the fluid receives a large heat flux from the heated wall. Thus, the thermophysical properties of helium gas were dependent on temperature and pressure. For the regions of $0°C < T_b < 3000°C$ and $P > 0.1$ MPa, they can be obtained by the following equations [21].

- Density [kg/m^3]; $\rho = P_{bar}/RT_{bk} - A(T_{bk})\rho^2 - B(T_{bk})\rho^3$

  where, P_{bar} [bar] $= 10^{-5} \times P$ [Pa]

  T_{bk} [K] $= T_b$ [°C] + 273.15

$$R = 2.07723 \times 10^{-2} \ [\mathrm{bar \cdot m^3/kgK}]$$

$$A(T_{bk}) = 4.5 \times 10^{-4} + 5.42/(1890 + T_{bk})$$

$$B(T_{bk}) = 1.7 \times 10^{-7} + 4.2 \times 10^{-3}/(1890 + T_{bk}) + 25.3/(1890 + T_{bk})^2$$

- Specific heat capacity [J/kgK] ; $c_p = 5193$

- Viscosity [Ns/m^2] ; $\mu = 3.78 \times 10^{-7} T_{bk}^{0.69} + 5 \times 10^{-7}/(0.52 + T_{bk}/569.6) + 2.67 \times 10^{-10} \rho^2$

- Thermal conductivity [W/mK] ;
  $\lambda = 2.97 \times 10^{-3} T_{bk}^{0.69} + 9.23 \times 10^{9} T_b/(T_b^5 + 4.29 \times 10^{14}) + 2.33 \times 10^{-4} \rho + 2.39 \times 10^{-6} \rho^2$

3.4 Results and Discussion

To verify the accuracy of the predicted Nu obtained by this numerical analysis using the standard k-ε model constants, first it was compared with the analytical value of Kays & Leung [2] under the following conditions; a concentric smooth annulus with a fully developed turbulent velocity profile, a heated inner wall, an insulated outer wall, Di/Do=0.8, Pr=0.7, and Re=10^4, 3x10^4 and 10^5. As shown in Fig. 8, the predicted Nu was in good agreement with their analytical value within an error of 5%. Thus, it was thought that the standard k-ε model constants could be applied up to a certain region of Re<10^4 even if the analytical model was different.

Figure 9 (a) shows the axial velocity distribution between the inner and outer walls. Here, the sector angle, θ, is 50°, the inlet average velocity, $u_{m,i}$, 10.5 m/s and the inlet average Re, $Re_{m,i}$, 5000. The shape of velocity distribution was almost similar from the inlet to the outlet in the flow direction. The velocity showed a maximum value at the center of the turbulence core region, and it was about 1.2 times higher than $u_{m,i}$. Figure 9 (b) shows the axial velocity distribution at θ =0° and $Re_{m,i}$=5000. The velocity decreased in comparison with θ=50° in Fig. 9 (a). Especially, just behind the spacer rib, it was quite small but not negative, and its maximum value was reduced down to about a half of u_{im}.

Figure 10 shows the axial velocity distribution at the center plane between the walls when 0°≤θ<60° and $Re_{m,i}$=5000. The influence of flow disturbance due to the spacer rib reached up to about θ=20° at the outlet section, along the flow separation shown as a dashed line. Just behind the spacer rib, a wake by the velocity defect appeared, and it recovered as

with the axial distance increased. On the other hand, the velocity distribution in the region of $20° < \theta < 60°$ was almost uniform in the flow direction.

Figure 11 shows the radial temperature distribution between the inner and outer walls when $Re_{m,i}$=5000. Where, Fig. 11 (a) is θ=50°, Fig. 11 (b) is θ=0°, and each line, such as the solid and broken lines, means the temperature distribution at an arbitrary axial location. In Fig.11 (a), the temperature in the turbulence core region decreases as y increased. At near inner wall, the temperature gradient was very sharp because of the large heat flux into the fluid. On the other side, the temperature distribution in Fig. 11 (b) received a strong the influence from the spacer rib because the fluid flow was disturbed in the vicinity of the spacer rib. In particular, the outer wall temperature increased around the spacer rib due to the generation of stagnation just before and behind the spacer rib. The author et al. [22] have already confirmed the existence of those using the flow visualization procedure.

A three-dimensional inner wall temperature distribution at $Re_{m,i}$=5000 is shown in Fig. 12. At θ=60° and θ=-60°, the T_{iw} was the lowest in the flow direction. The reason is as follows: The reduction of channel cross-section due to the spacer rib increases the velocity, and the velocity becoming maximum at the center position between the ribs in the circumferential direction, with the blockage also producing turbulence. Consequently, the heat transfer is improved. In addition, T_{iw} increased from θ=60° and θ=-60° as it approached θ=0° in the circumferential direction. Furthermore, the T_{iw} at θ=0° was influenced by the wake flow generated behind the spacer rib and was greatly reduced at the certain position just behind it. Thus, it was expected the heat transfer coefficient was augmented to a considerable extent at that position.

Figure 13 shows the variations of predicted Nu before and after the spacer rib in the flow direction. Where, the solid, broken and dashed lines represent the Nu distributions corresponding to $Re_{m,i}$ =5000, 10000 and 20000, respectively. The Nu increases with Re, however, the shape of the Nu distribution was almost equal for each Re. A gradually decrease in the Nu could be seen from the inlet to the outlet sections. The reason is as follows: In Eq. (3), not only λ increases with temperature but also the rate of T_{iw}-T_{bm} increases along the flow direction. Here, although T_{iw} and T_{bm} rise proportionally with the axial distance from the channel inlet, the rate of temperature rise of T_{iw} per unit length is larger than that of T_{bm}, so that the difference between T_{iw} and T_{bm} is extended. From the inlet to the outlet sections, the Nu varied from 15 to 11 at $Re_{m,i}$=5000, from 22 to 18 at 10000, and from 36 to 31 at 20000. Furthermore, it was considered that the reason why the Nu increased in the vicinity of the spacer rib was due to the influence of the heat transfer

augmentation resulting from the rib, as implied from the inner wall temperature distribution in Fig. 12.

Figure 14 shows the comparison between the predicted average Nusselt number, Nu_m, and Eq. (4). Where, circular symbol indicates the prediction, solid line the value of Eq. (4), and broken and dashed lines 10% higher and lower values from Eq. (4), respectively. In the region of $5000 \leq Re \leq 20000$, the Nu_m agreed well with Eq. (4) within a relative error of 10%. Thus, there was some concern about this numerical analysis result having sufficient accuracy and simulating well the turbulent heat transfer performance of the spacer ribbed fuel rod for the HTTR. However, at Re=3000, the Nu_m was much higher than the value of Eq. (4), with a difference of 51%. This reason is that the k-ε model constans exceeded their application range. JAERI has a plan in which the HTTR core will be operated in the region of $3000 < Re < 10000$. From this viewpoint, it is important to simulate perfectly the heat transfer characteristics of the spacer ribbed fuel rod for the region of $Re < 5000$. In this respect, the author plans to give more consideration to the low Re turbulent region.

4. Concluding Remarks

The turbulent heat transfer performance of the fuel rod with three-dimensional trapezoidal spacer ribs for the HTTR was predicted numerically and investigated experimentally for various Re under the conditions of high temperature and high pressure. These results are summarized below.

1. The turbulent heat transfer coefficients of the fuel rod were 18 to 80% higher than the values of the concentric smooth annulus in the region of $Re > 2000$, and it was correlated with Eq.(4) and showed good agreement.

2. The predicted average Nu agreed well with Eq. (4) within a relative error of 10% in the region of $Re \geq 5000$. Thus, it could be verified that the numerical analysis results had sufficient accuracy.

3. The numerical prediction clarified quantitatively the effects of the heat transfer augmentation by the spacer rib and the axial velocity increase by a reduction of the annular channel cross-section.

Acknowledgment

The author would like to express his sincere gratitude to Dr. Akino for his very helpful suggestions regarding the numerical simulation, and also Drs. Hino and Miyamoto for their consideration concerning the evaluation of data. The FLUENT program used to the present study was provided by Ryutai Consultant Co., Ltd. in Japan. The author would also like to express his thanks to Dr. Mouri, president of the company and to his colleagues.

References

[1] Takase, K., Maruyama, S., Hino, R., Hishida, M., Izawa, N. and Shimomura, H., Experimental studies on thermal and hydraulic performance of fuel stack on VHTR, (I) Test results of HENDEL single-channel test rig with uniform heat flux distribution (in Japanese), J. Atomic Energy Society of Japan, 28, 5(1986)428-435.

[2] Kays, W. M., and Leung, E. Y., Heat transfer in annular passages - hydrodynamically developed turbulent flow with arbitrarily prescribed heat flux, Int. J. Heat Mass Transfer, 6(1962)537-557.

[3] Dalle Donne, M., and Meerwald, E., Heat transfer and friction coefficients for turbulent flow of air in smooth annuli at high temperature, Int. J. Heat Mass Transfer, 16(1973)787-809.

[4] Dalle Donne, M., and Meyer, L., Turbulent convective heat transfer from rough surfaces with two-dimensional rectangular ribs, Int. J. Heat Mass Transfer, 20(1977)583-620.

[5] Wilson, N. W., and Medwell, J. O., An analysis of heat transfer for fully developed turbulent flow in concentric annuli, J. Heat Transfer, (1968)43-50.

[6] Hassan, M. A., and Rehme, K., Heat transfer near spacer grids in gas-cooled rod bundles, Nuclear technology, 52(1981)401-414.

[7] Takase, K., Hino, R., Miyamoto, Y., and Akino, N., Experimantal and numerical studies on heat transfer and flow characteristics of a fuel rod with transverse square ribs, Proceedings of the 10th International Heat Transfer Conference, England, Vol.3, (1994)245-250.

[8] Han, J. C., Glicksman, L. R., and Rohsenow, W. M., An investigation of heat transfer and friction for rib-roughened surfaces,, Int. J. Heat Mass Transfer, 21(1978)1143-1156.

[9] Takase, K., Experimantal and analytical studies on turbulent heat transfer performance of a fuel rod with spacer ribs for high temperature gas-cooled reactors, Nuclear Engineering and Design, to be published.

[10] Goldsmith, A., Waterman, T. E., and Hirschborn, H. J., Handbook of Thermophysical Properties of Solid Materials: Vol.1, (MACMILLAN, New York, 1961), pp.127-131.

[11] Makino, T., Kunitomo, T., and Mori, T., Study on characteristics of thermal radiation of heat resisting alloy with high temperature (in Japanese), J. Japan Society Mechanical Engineering, 49-441(1983)1040-1047.

[12] Fujii, S., Hishida, M., Kawamura, H., and Akino, N., Heat transfer in annular channels under the high heat flux conditions (in Japanese), 17the Japan Heat Transfer Symposium, A213(1980)97-99.

[13] Kays, W. M., and Crawford, M. E., Convective Heat and Mass Transfer (third edition, McGRAW-HILL, New York, 1993), p123.

[14] Patankar, S.V., Liu, C.H., and Sparrow, E. M., Fully developed flow and heat transfer in ducts having streamwise-periodic variations of cross-sectional area, J. Heat Transfer, 99(1977)180-186.

[15] Jones,W.P. and Launder, B.E., The prediction of laminarization with a two-equation model of turbulence, Int. J. Heat Mass Transfer, 15(1972)301-314.

[16] Launder, B.E. and Spalding, D. B., The numerical computation of turbulent flows, Computer Methods in Applied Mechanics and Engineering, 3(1974)269-289.

[17] FLUENT User's Guide Version 4, Fluent Inc., (1991).

[18] Patankar, S. V., Numerical Heat Transfer and Fluid Flow, (McGRAW-HILL, New York, 1980), pp.130-136.

[19] Hackbusch, W., Multi-grid Methods and Applications, (Springer-Verlag, New York, 1985).

[20] Mastin, C. W. and Thompson, J. F., Transformation of three-dimensional regions onto rectangular regions by elliptic systems, Numerische Mathematik, 29 (1978)397-407.

[21] Harth, R., and Hammeke, K., Thermodynamische Stoffwerte von HELIUM im Bereich von 0 bis 3000°C und 0.2 bis 200 bar, Julich National Laboratory Report, JUL-666-RB (August, 1969).

[22] Takase, K., Hino, R., Maruyama, S., Akino, N., Kunugi, T., and Kawamura, H., A flow visualization around an obstacle in a parallel channel (in Japanese), J. Visualization Society of Japan, 6-22(1986)323-326.

Nomenclature

C : van Driest's constant
c_p : specific heat
C_μ, $C_{\epsilon 1}$, $C_{\epsilon 2}$: turbulence model constants, 0.09, 1.44, 1.92, respectively.
De : hydraulic diameter, Do-Di
Di, Do : fuel rod and outer tube diameters
E : log-law constant
f : friction factor
G : flow rate
H : channel height, De/2
k : turbulent kinematic energy

L : axial distance
Nu : Nusselt number
P : pressure
p : square rib pitch
Δp : pressure loss
Pr, Pr_t : Prandtl number, turbulent Prandtl number, Pr_t=0.9
q, q^+ : heat flux, dimensionless heat flux
R : gas constant
Re : Reynolds number, u_m De /v
T : temperature
u, v, w : axial, radial and circumferential velocities
x, y, z : axial, radial and circumferential coordinates
y : distance from the wall

Greek symbols
β : mean pressure gradient
ε : dissipation
γ : mean rate of temperature rise
κ : von Karman's constant
λ : thermal conductivity
μ, μ_t, μ_{eff} : viscosity, turbulent viscosity, effective viscosity, $\mu_t=C_\mu \rho (k^2/\varepsilon)$ and $\mu_{eff}=\mu+\mu_t$
ν : kinematic viscosity
ρ : density
σ_k, σ_ε : turbulent Prandtl number for k and ε, σ_k=1 and σ_ε=1.3

Subscripts
b : bulk
c : convection
e : heat generation
f : spacer ribbed fuel rod
i : inlet
l : laminar
m : mean or average
o : outlet
P : periodic part
p : near wall
r : radiation
s : smooth anulus
t : turbulent
tr : transition
w : wall

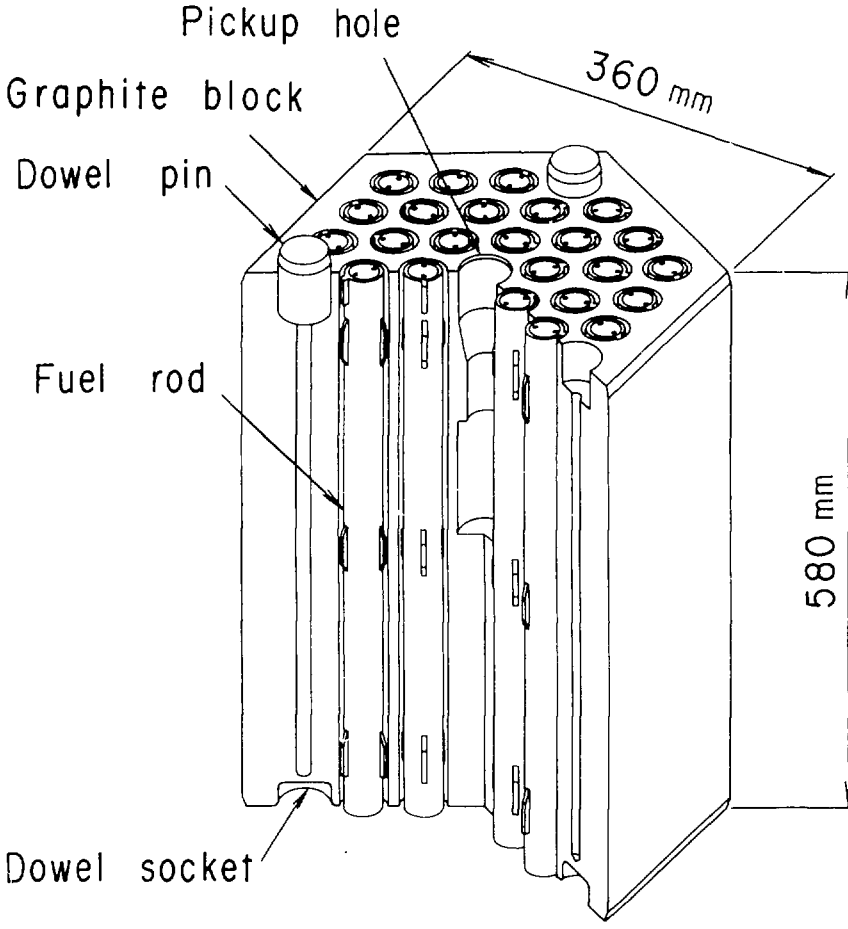

Fig. 1 The HTTR fuel element

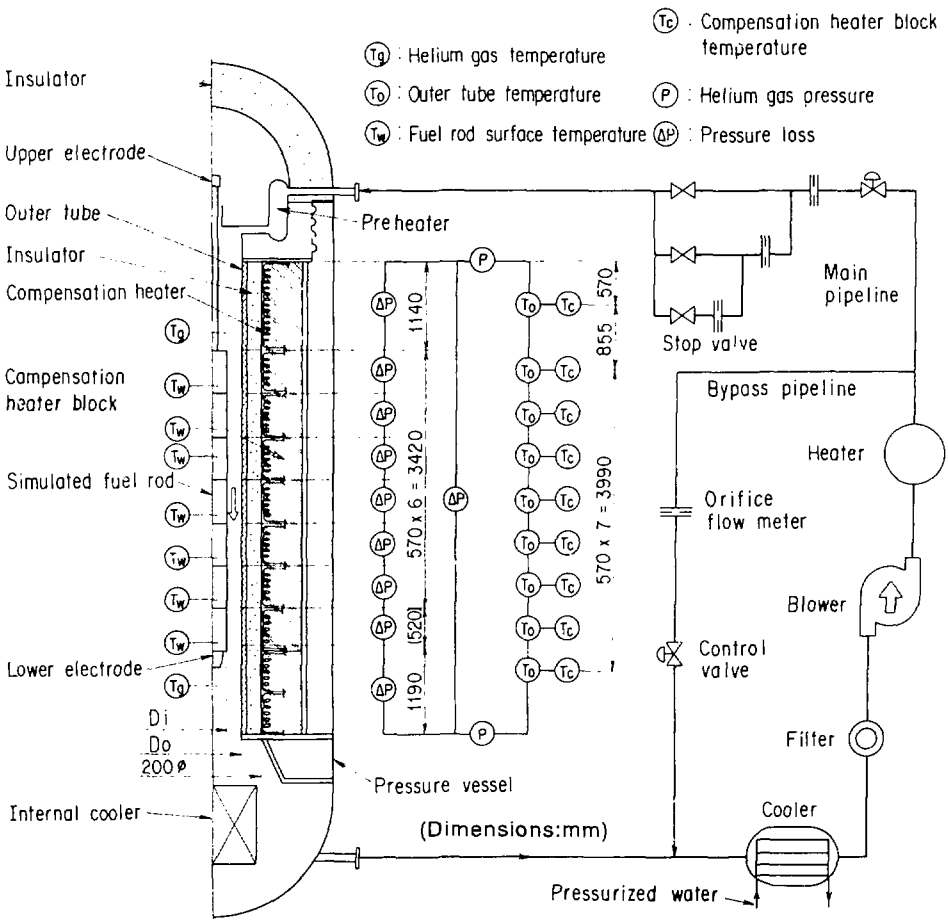

Fig. 2 Schematic drawing of a test rig and measuring positions

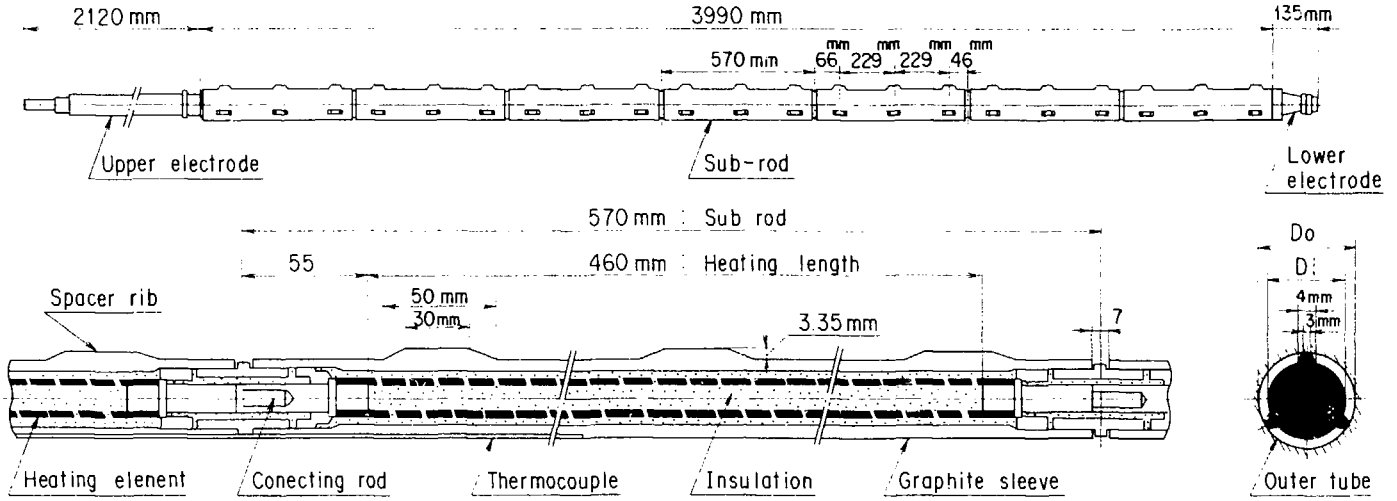

Fig. 3 Schematic drawing of the simulated fuel rod

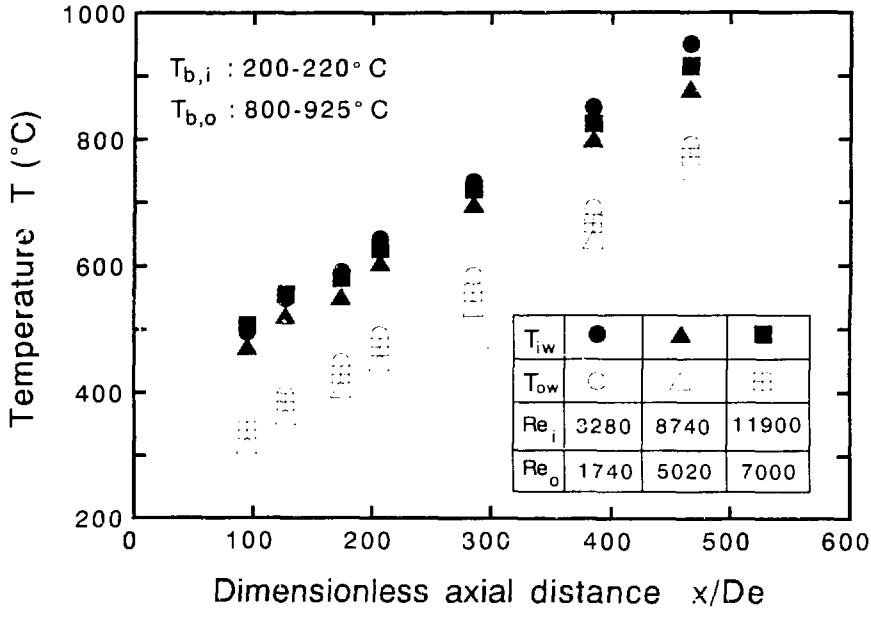

Fig. 4 Axial temperature distribution

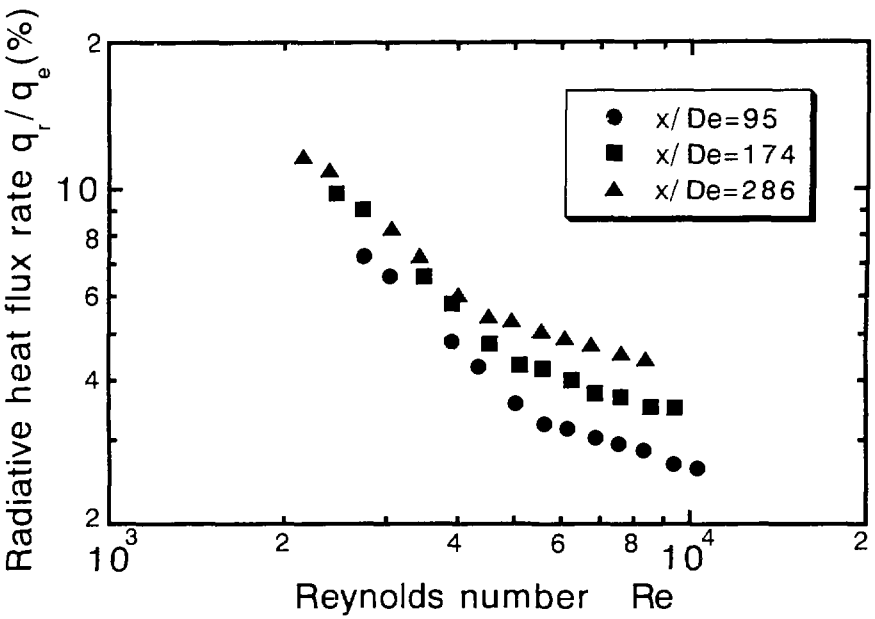

Fig. 5 Relation between the radiative heat transfer and Re

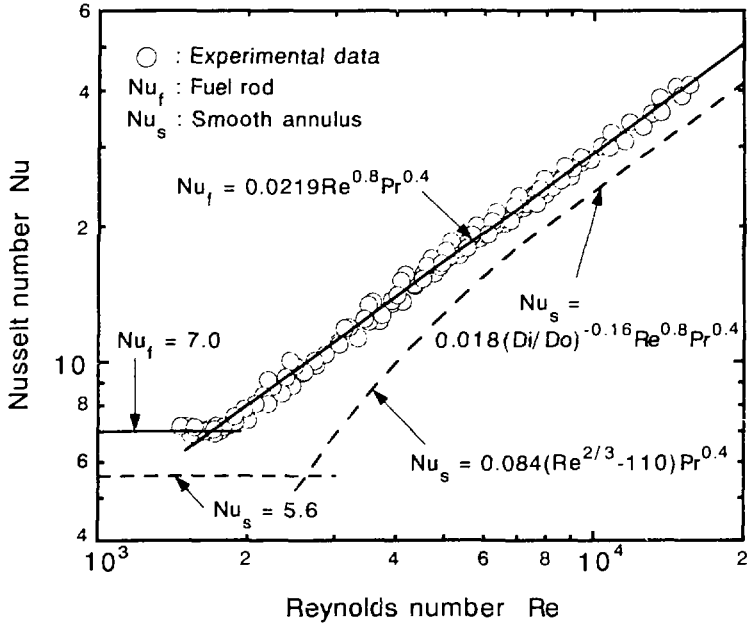

Fig. 6 Relation between Nu and Re

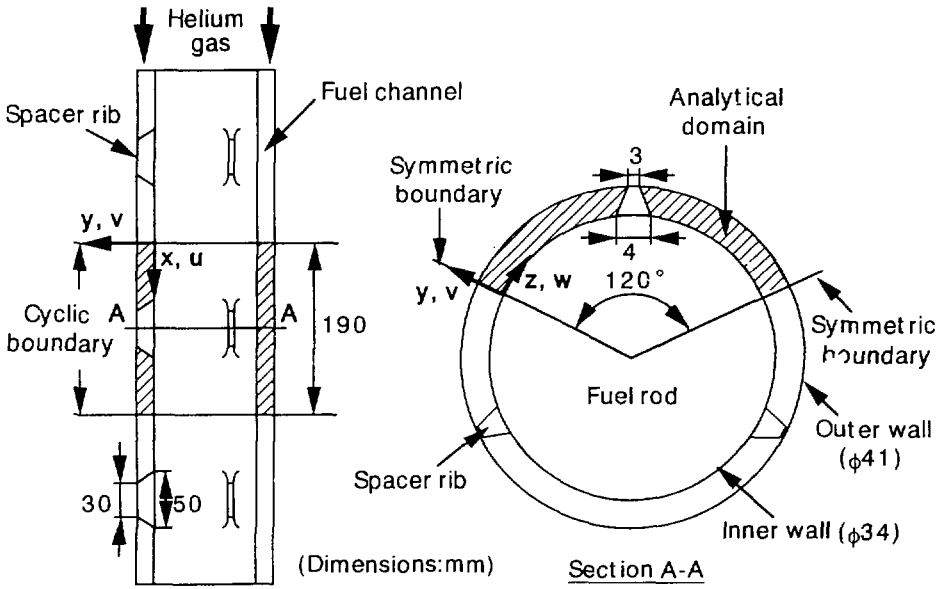

Fig. 7 Analytical model and boundary conditions

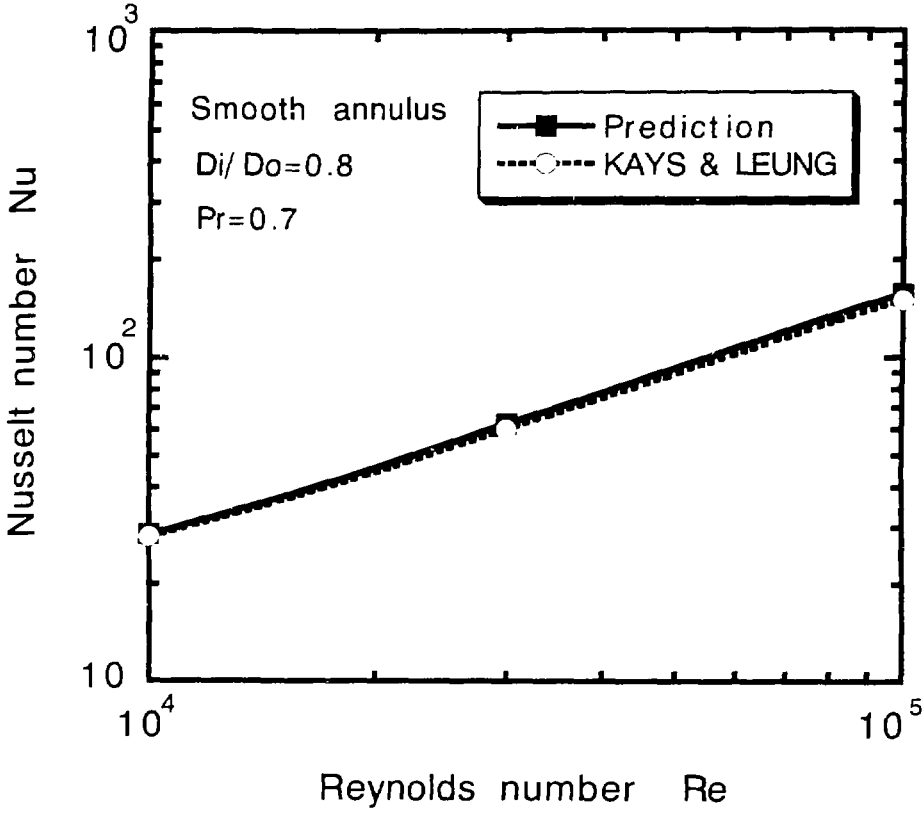

Fig. 8 Comparison between the predicted Nu and the analytical value under the condition of a concentric smooth annulus with a fully developed axial velocity profile

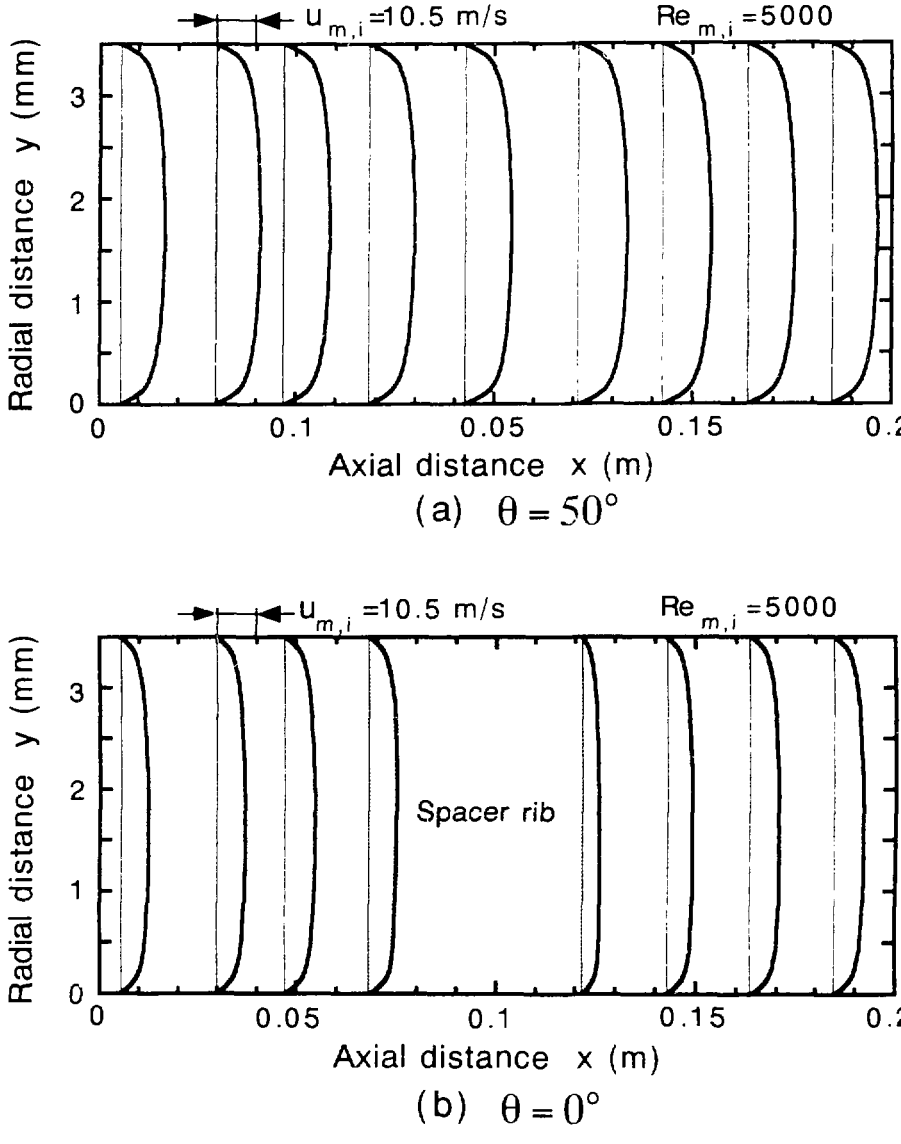

Fig. 9 Axial velocity distribution between the inner and the outer walls

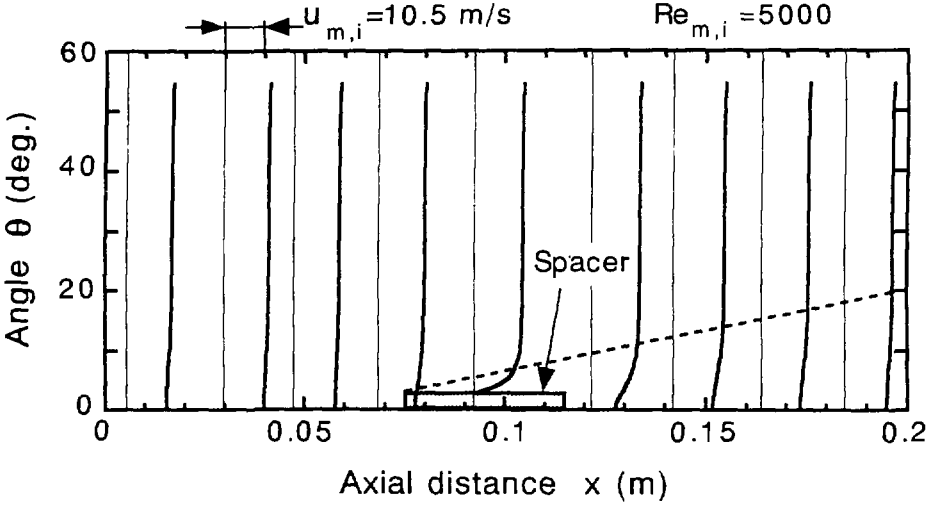

Fig. 10 Axial velocity distribution at the center plane between the walls when $0° \leqq \theta < 60°$

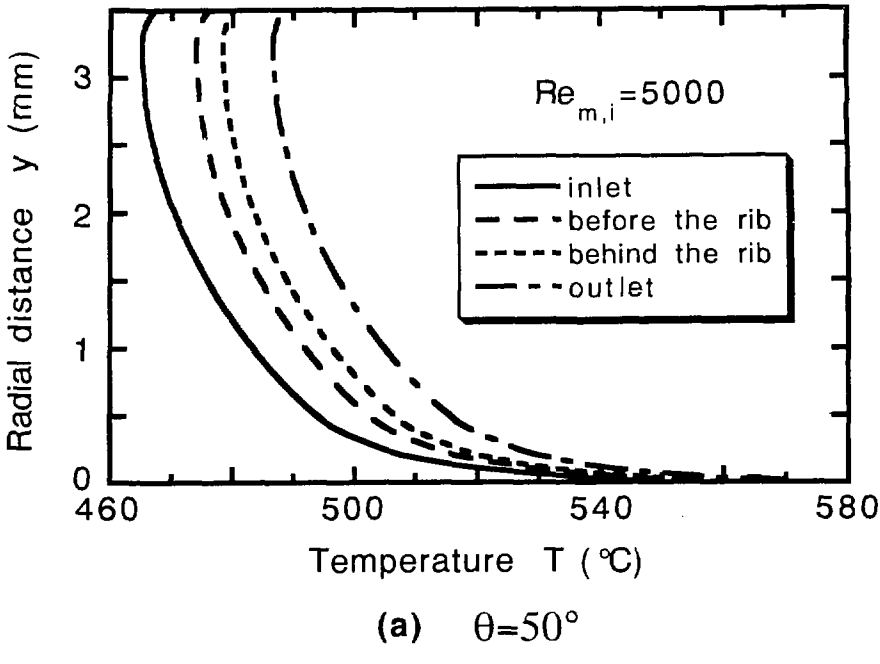

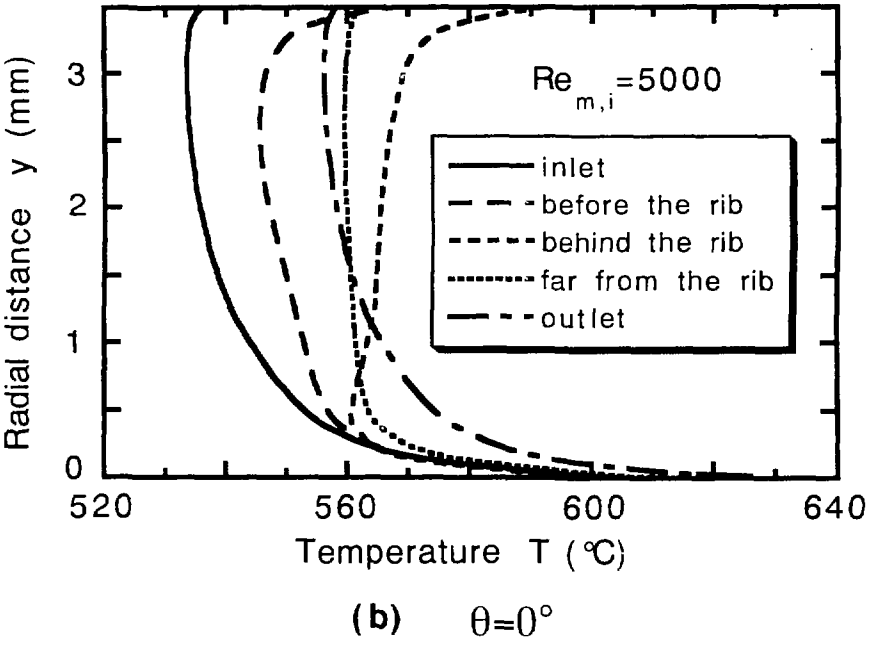

Fig. 11 Axial temperature distribution between the inner and outer walls

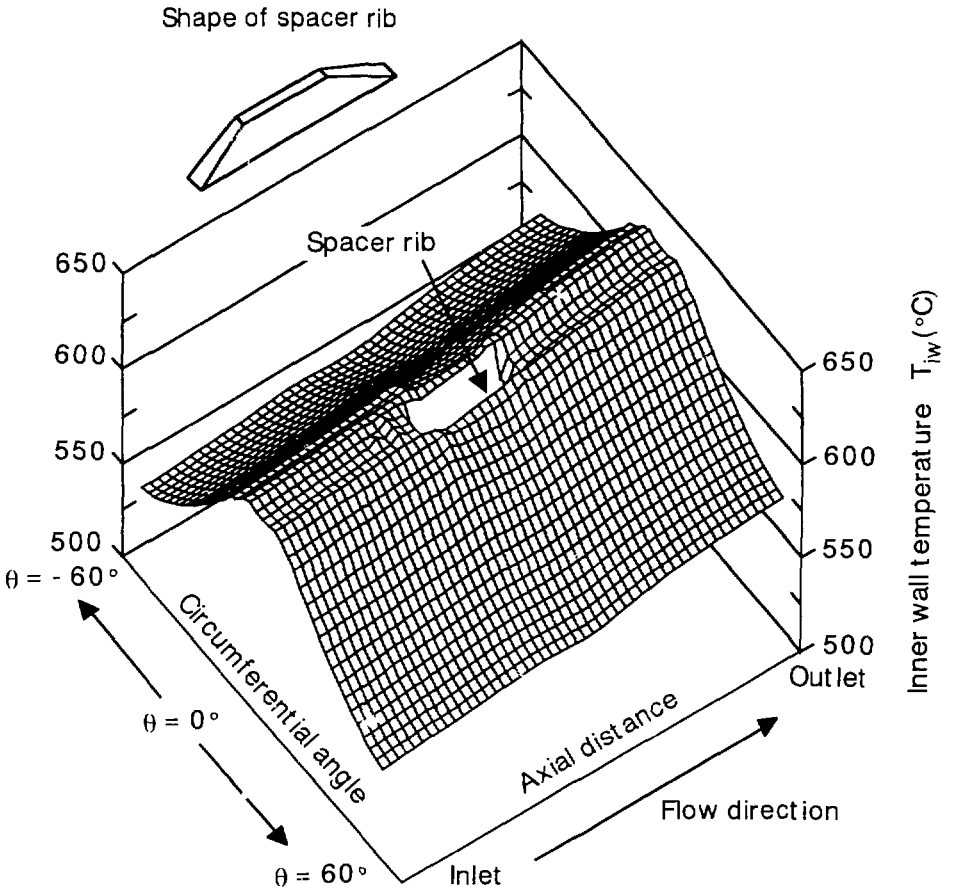

Fig. 12 Three-dimensional inner wall temperature distribution at $Re_{m,i}$ =5000

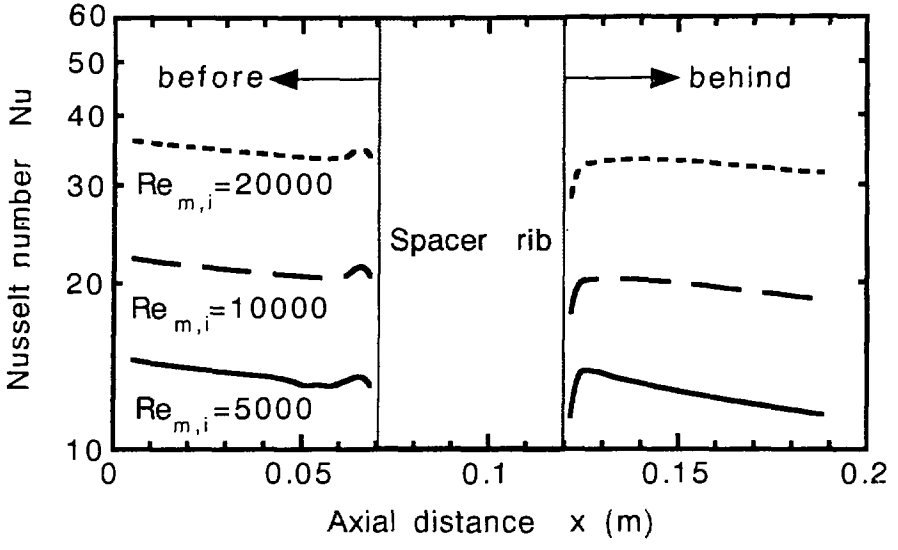

Fig. 13 Variations of the predicted Nu before and behind the spacer rib

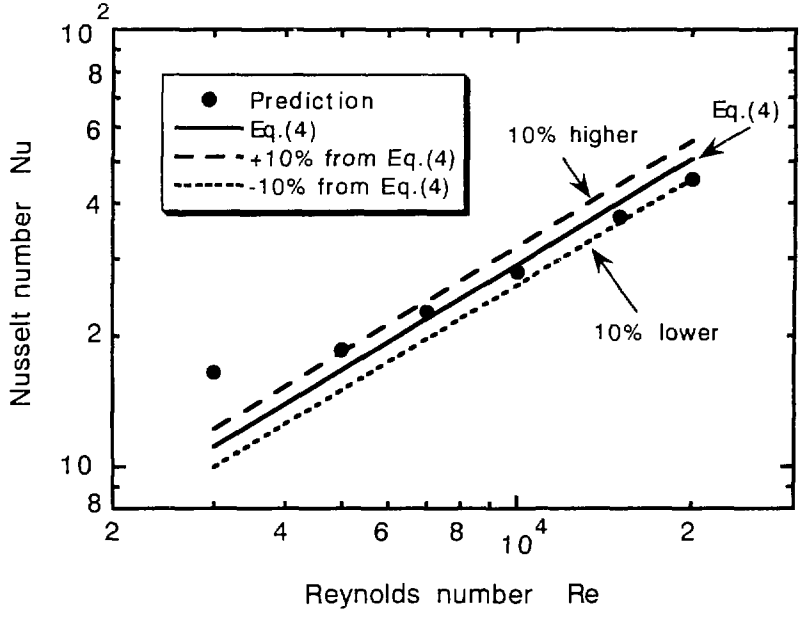

Fig. 14 Comparison between the predicted average Nu and the empirical correlation

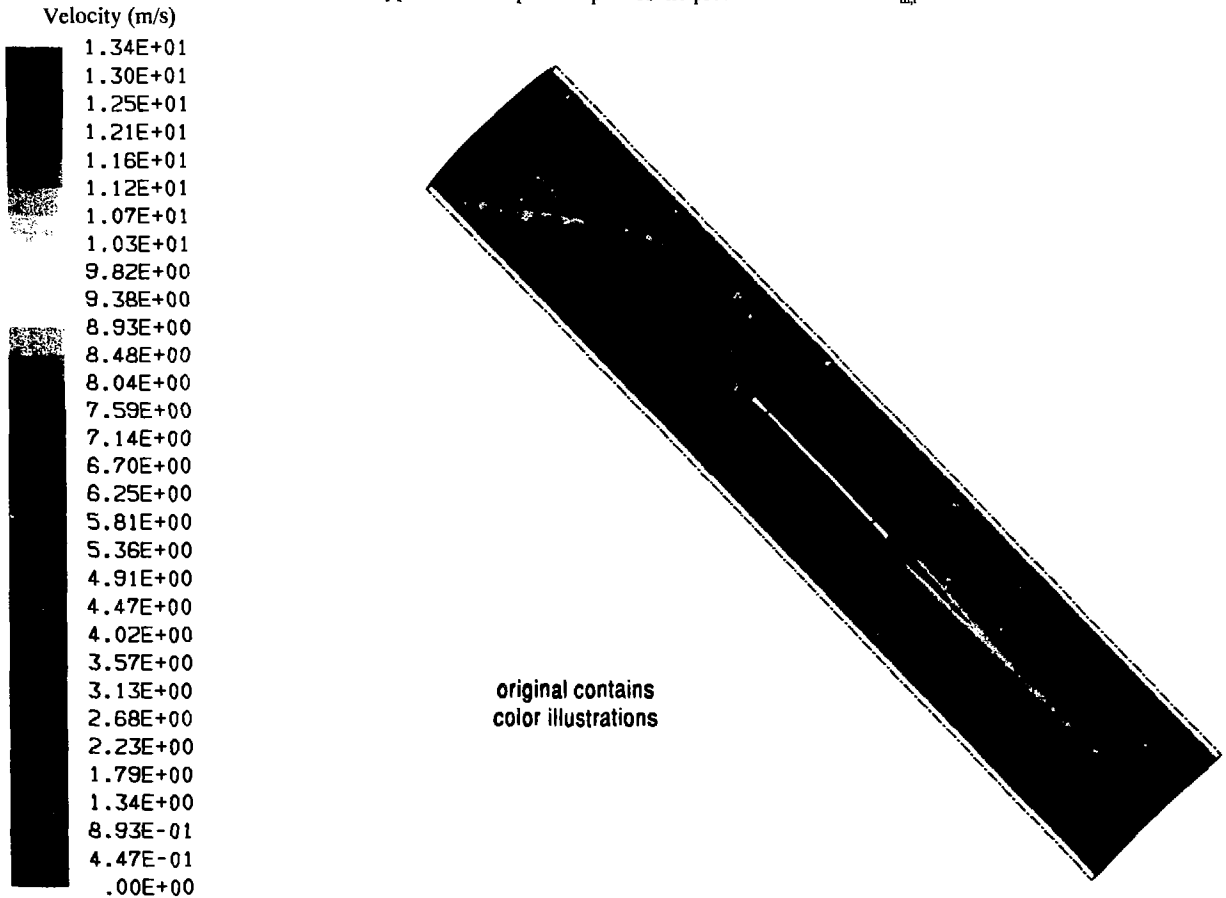

Fig. A1 Color filled axial velocity distribution at the center plane between the inner and outer walls

Where, a color-bar at the left-hand side represents the velocity rate. The axial velocity increased at the spacer rib region due to the reduction of the annular channel cross-section, and also the wake flow appeared behind the spacer rib along the flow direction.

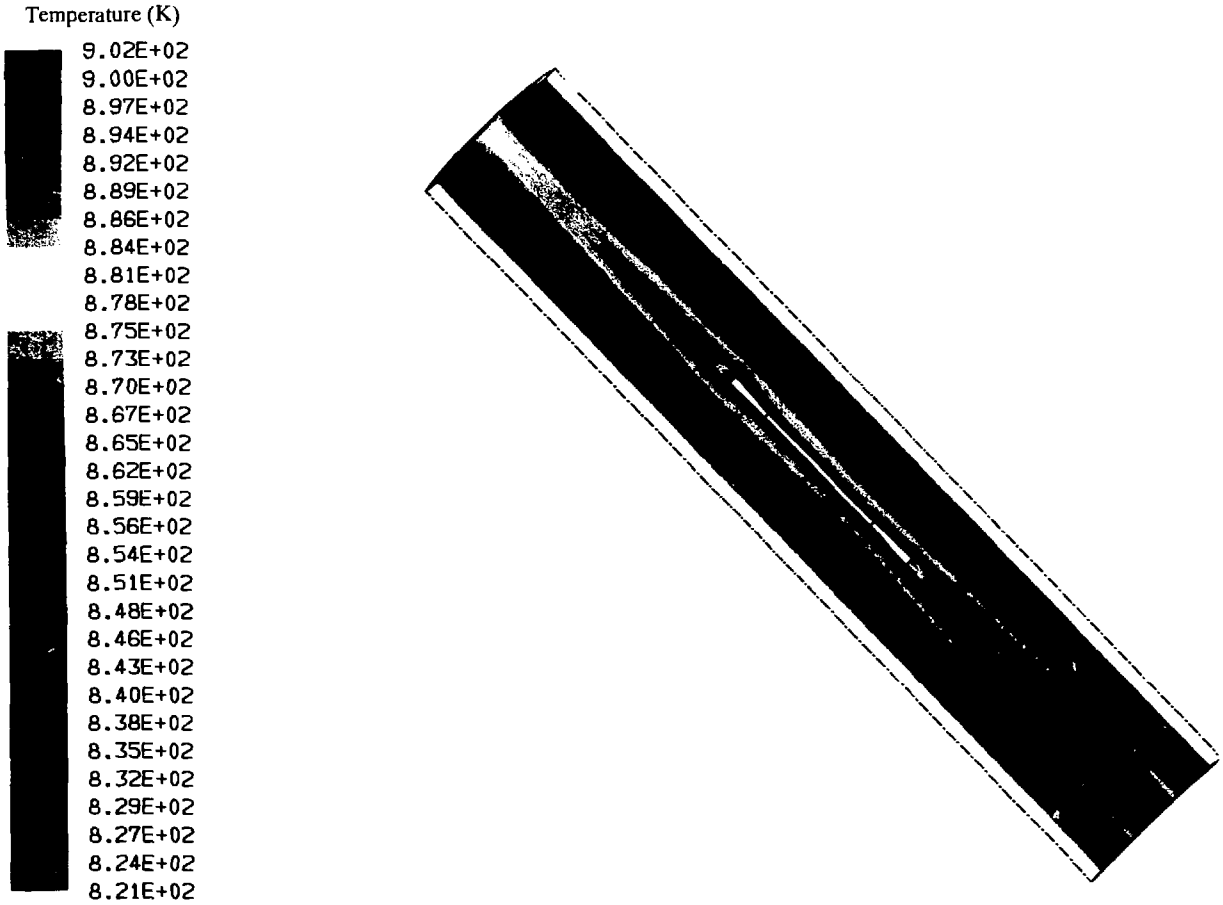

Fig. A2 Color filled inner wall temperature distribution

Where, a color-bar represents the temperature rate. The wall temperature received a strong influence from the spacer rib. In particular, the wall temperature behind the spacer rib was influenced by the wake flow and its influence was observed along a row of the spacer ribs.

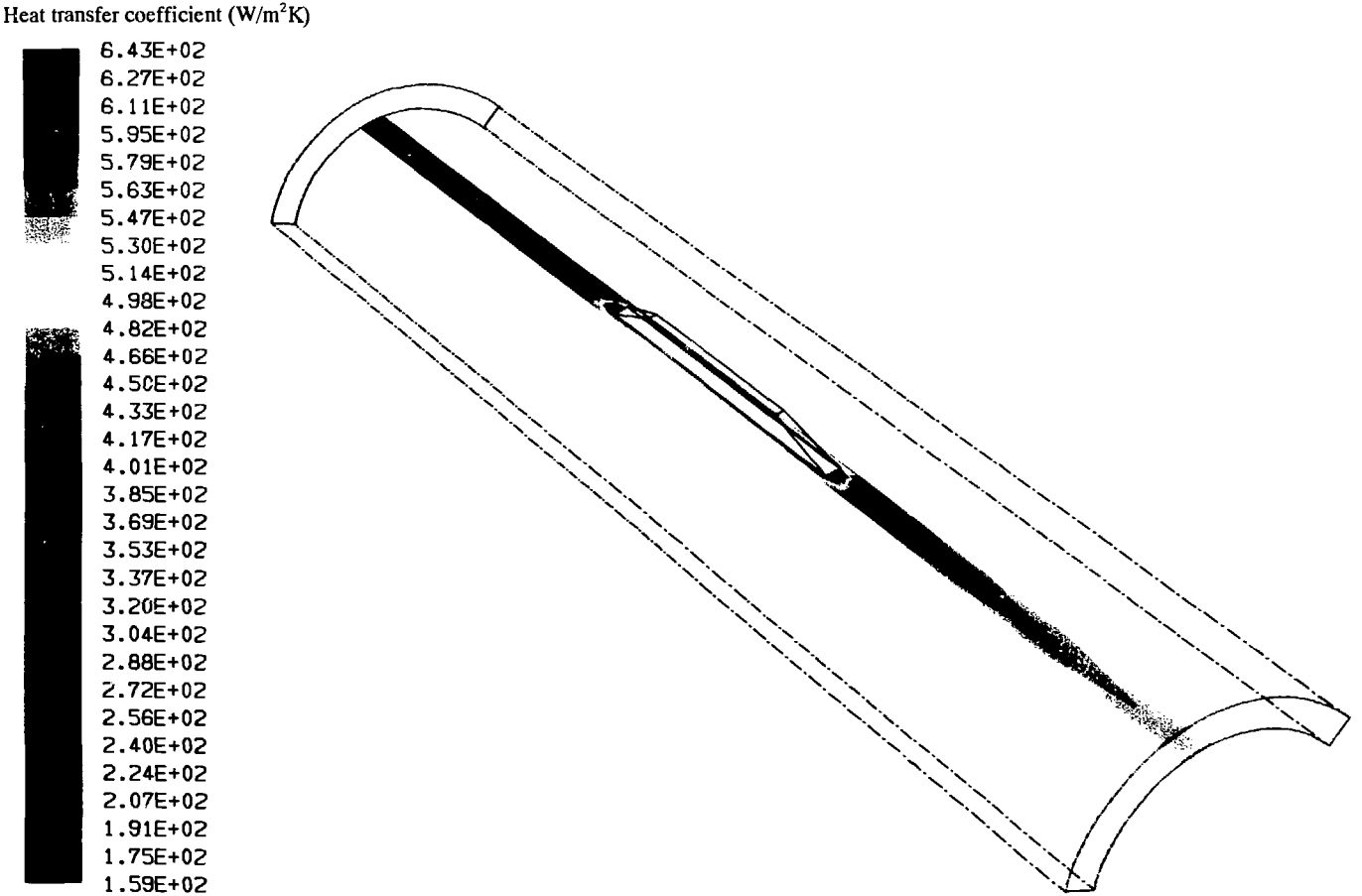

Fig. A3 Color filled heat transfer coefficient distribution before and after the spacer rib

Where, a color-bar represents the heat transfer coefficient. The heat transfer coefficient was high at the channel inlet, low at the outlet, and very small around the spacer rib. Furthermore, it increased at the certain position behind the spacer rib because of the effect of the heat transfer augmentation by roughness.

国際単位系 (SI) と換算表

表1　SI基本単位および補助単位

量	名称	記号
長さ	メートル	m
質量	キログラム	kg
時間	秒	s
電流	アンペア	A
熱力学温度	ケルビン	K
物質量	モル	mol
光度	カンデラ	cd
平面角	ラジアン	rad
立体角	ステラジアン	sr

表2　SIと併用される単位

名称	記号
分，時，日	min，h，d
度，分，秒	°，′，″
リットル	l，L
トン	t
電子ボルト	eV
原子質量単位	u

1 eV　1.60218×10^{-19} J

1 u　1.66054×10^{-27} kg

表3　固有の名称をもつSI組立単位

量	名称	記号	他のSI単位による表現
周波数	ヘルツ	Hz	s^{-1}
力	ニュートン	N	m·kg/s^2
圧力，応力	パスカル	Pa	N/m^2
エネルギー，仕事，熱量	ジュール	J	N·m
仕事率，放射束	ワット	W	J/s
電気量，電荷	クーロン	C	A·s
電位，電圧，起電力	ボルト	V	W/A
静電容量	ファラド	F	C/V
電気抵抗	オーム	Ω	V/A
コンダクタンス	シーメンス	S	A/V
磁束	ウェーバ	Wb	V·s
磁束密度	テスラ	T	Wb/m^2
インダクタンス	ヘンリー	H	Wb/A
セルシウス温度	セルシウス度	℃	
光束	ルーメン	lm	cd·sr
照度	ルクス	lx	lm/m^2
放射能	ベクレル	Bq	s^{-1}
吸収線量	グレイ	Gy	J/kg
線量当量	シーベルト	Sv	J/kg

表4　SIと共に暫定的に維持される単位

名称	記号
オングストローム	Å
バーン	b
バール	bar
ガル	Gal
キュリー	Ci
レントゲン	R
ラド	rad
レム	rem

1 Å = 0.1 nm = 10^{-10} m

1 b = 100 fm^2 = 10^{-28} m^2

1 bar = 0.1 MPa = 10^5 Pa

1 Gal = 1 cm/s^2 = 10^{-2} m/s^2

1 Ci = 3.7×10^{10} Bq

1 R = 2.58×10^{-4} C/kg

1 rad = 1 cGy = 10^{-2} Gy

1 rem = 1 cSv = 10^{-2} Sv

表5　SI接頭語

倍数	接頭語	記号
10^{18}	エクサ	E
10^{15}	ペタ	P
10^{12}	テラ	T
10^{9}	ギガ	G
10^{6}	メガ	M
10^{3}	キロ	k
10^{2}	ヘクト	h
10^{1}	デカ	da
10^{-1}	デシ	d
10^{-2}	センチ	c
10^{-3}	ミリ	m
10^{-6}	マイクロ	μ
10^{-9}	ナノ	n
10^{-12}	ピコ	p
10^{-15}	フェムト	f
10^{-18}	アト	a

（注）

1. 表1～5は「国際単位系」第5版，国際度量衡局 1985年刊行による．ただし，1 eVおよび1 uの値はCODATAの1986年推奨値によった．
2. 表4には海里，ノット，アール，ヘクタールも含まれているが日常の単位なのでここでは省略した．
3. barは，JISでは流体の圧力を表わす場合に限り表2のカテゴリーに分類されている．
4. EC閣僚理事会指令ではbar，barnおよび「血圧の単位」mmHgを表2のカテゴリーに入れている．

換　算　表

力	N (=10^5 dyn)	kgf	lbf
	1	0.101972	0.224809
	9.80665	1	2.20462
	4.44822	0.453592	1

粘度　1 Pa·s (N·s/m^2) = 10 P (ポアズ) (g/(cm·s))

動粘度　1 m^2/s = 10^4 St (ストークス) (cm^2/s)

圧力	MPa (=10 bar)	kgf/cm^2	atm	mmHg (Torr)	lbf/in^2 (psi)
	1	10.1972	9.86923	7.50062×10^3	145.038
	0.0980665	1	0.967841	735.559	14.2233
	0.101325	1.03323	1	760	14.6959
	1.33322×10^{-4}	1.35951×10^{-3}	1.31579×10^{-3}	1	1.93368×10^{-2}
	6.89476×10^{-3}	7.03070×10^{-2}	6.80460×10^{-2}	51.7149	1

エネルギー・仕事・熱量	J (=10^7 erg)	kgf·m	kW·h	cal (IT国際蒸気表)	Btu	ft·lbf	eV
	1	0.101972	2.77778×10^{-7}	0.238889	9.47813×10^{-4}	0.737562	6.24150×10^{18}
	9.80665	1	2.72407×10^{-6}	2.34270	9.29487×10^{-3}	7.23301	6.12082×10^{19}
	3.6×10^6	3.67098×10^5	1	8.59999×10^2	3412.13	2.65522×10^6	2.24694×10^{25}
	4.18605	0.426858	1.16279×10^{-6}	1	3.96759×10^{-3}	3.08747	2.61272×10^{19}
	1055.06	107.586	2.93072×10^{-4}	252.042	1	778.172	6.58515×10^{21}
	1.35582	0.138255	3.76616×10^{-7}	0.323890	1.28506×10^{-3}	1	8.46233×10^{18}
	1.60218×10^{-19}	1.63377×10^{-20}	4.45050×10^{-26}	3.82743×10^{-20}	1.51857×10^{-22}	1.18171×10^{-19}	1

1 cal = 4.18605 J (計量法)

4.184 J　(熱化学)

4.1855 J　(15 ℃)

4.1868 J (国際蒸気表)

仕事率　1 PS (仏馬力)

75 kgf·m/s

735.499 W

放射能	Bq	Ci
	1	2.70270×10^{-11}
	3.7×10^{10}	1

吸収線量	Gy	rad
	1	100
	0.01	1

照射線量	C/kg	R
	1	3876
	2.58×10^{-4}	1

線量当量	Sv	rem
	1	100
	0.01	1

(86年12月26日現在)

NUMERICAL PREDICTION ON TURBULENT HEAT TRANSFER OF A SPACER RIBBED FUEL ROD FOR HIGH TEMPERATURE GAS-COOLED REACTORS